Coherent dynamics of thalamic head-direction neurons irrespective of input.

Guillaume Viejo [1, 2, +,*] , Sofia Skromne Carrasco [1, +] and Adrien Peyrache [1,*]

1- Montreal Neurological Institute, McGill University, Montreal, QC, Canada

2- Center for Computational Neuroscience, Flatiron Institute, New York, NY, USA

+-These authors contributed equally to the work.

*Corresponding authors: Guillaume Viejo, gviejo@flatironinstitute.org; Adrien Peyrache, adrien.peyrache@mcgill.ca

Abstract

While the thalamus is known to relay and modulate sensory signals to the cortex, whether it also participates in active computation and intrinsic signal generation remains unresolved. The anterodorsal nucleus of the thalamus broadcasts the head-direction (HD) signal, which is generated in the brainstem, particularly in the upstream lateral mammillary nucleus, and thalamic HD cells remain coordinated even during sleep. Here, by recording and manipulating neuronal activity along the mammillary–thalamic–cortical pathway, we show that coherence among thalamic HD cells persists even when their upstream inputs are decorrelated, particularly during non-Rapid Eye Movement sleep. These findings suggest that thalamic circuits are sufficient to generate and maintain coherent population dynamics in the absence of structured input.

Introduction

For much of modern neuroscience, the thalamus has been regarded primarily as a relay hub: a subcortical structure that gates and modulates the flow of sensory information to the cortex [1,2].

Yet, recent studies have begun to reveal that thalamic circuits may participate in more complex operations—including state-dependent modulation, attention, and memory-related processes—raising the question of whether the thalamus is capable of intrinsic computation and signal generation [3–8]. Whether this generative potential extends to structured population dynamics in the absence of external input remains unresolved.

Transitions between brain states—such as wakefulness, Rapid Eye Movement (REM) sleep, and non-REM sleep—are accompanied by widespread changes in how sensory information is routed and processed through thalamocortical circuits. One of the most striking of these changes is the shift from a desynchronized state—characteristic of wakefulness and REM sleep, both driven by brainstem structures—to the synchronized dynamics of non-REM sleep, dominated by thalamocortical activity patterns [15–19]. Studying how internal representations reorganize across these states is often hindered by the high dimensionality of sensory inputs [20–22]. In contrast, the head-direction (HD) system, which encodes an animal's orientation in the horizontal plane [11,12,23,24], provides a low-dimensional, interpretable signal. This enables near-perfect decoding of the system's internal state, independent of external input.

The HD signal is crucial for navigation [25–28] and is represented by HD cells, each tuned to a specific direction of the animal's head. It is conveyed to the cortex by the anterodorsal nucleus of the thalamus (ADN), where a vast majority of neurons are modulated by HD [9,10,29]. ADN-HD cells maintain their mutual coordination both during REM and non-REM sleep [10,13,14], a brain state during which sensory inputs are largely absent. This persistent coordination is consistent with the notion of an internally generated, attractor-driven system [13,30–33]. Yet, whether the coherence of the HD signal is maintained by similar mechanisms across brain states remains unclear.

It has been proposed that the lateral mammillary nucleus (LMN), the main input to the ADN, acts as a central component of the HD signal generator circuit [11,34,35]. The ADN projects mainly to the postsubiculum (PSB), a cortical area where neurons are also strongly modulated by HD [10,23,36], which, in turn, projects back to the LMN [37,38].

Here, we investigated the ensemble organization of LMN activity across brain states and its relationship to ADN dynamics. During non-REM sleep, the coordination among LMN-HD cells was significantly reduced, while simultaneously recorded ADN neurons maintained the same level of mutual coherence as during wakefulness. Silencing the PSB totally abolished LMN-HD cell coordination, while the structure of ADN-HD cell activity was spared, indicating the crucial role of the PSB→LMN projection in maintaining some level of coordination in the LMN during non-REM sleep. These observations suggest that the thalamocortical HD circuit can support the emergence of structure activity independently of its afferent input.

59 # Results

60 **Coherence of HD cell population activity is maintained in the AD during non-REM, but**
61 **not in the LMN.**

62 To investigate the origin of structured activity in the ADn during sleep [10,13,14], mice were
63 chronically implanted with high-density silicon probes targeting the LMN (n = 11), ADn (n = 4),
64 or both (n = 8) (Figure 1A–C; Supp. Figure 1). We recorded a total of 546 HD cells in the LMN
65 and 265 in the ADn (Supp. Figure 2A-B). Mice explored a circular environment and were
66 allowed to sleep before and after exploration.

67 As expected, during wakefulness, HD population activity accurately tracked the animal's head
68 direction, forming a well-defined "activity packet". The structure of HD cell activity was
69 maintained in both structures during REM sleep (Supp. Figure 2C), suggesting that during
70 activated states of the brain, similar processes are at play in the generation of a coherent HD
71 signal [10,14,36].

72 During non-REM sleep, however, dynamics differed strikingly between the two structures
73 (Figure 1D). As previously reported, the ADN-HD cell population remained highly structured,
74 with activity packets resembling those observed during wake. In contrast, LMN-HD population
75 activity was less structured with respect to the cells' preferred direction (Figure 1D). The activity
76 of example HD cells from both regions further illustrates this difference (Figure 1E). HD cells in
77 the ADN with overlapping tuning curves during wake continued to fire together during non-
78 REM, while those with opposite tuning did not. In the LMN, however, cells with opposite
79 preferred directions unexpectedly showed frequent co-firing during non-REM.

To quantify this phenomenon, we computed pairwise coupling (i.e., Pearson's correlation of binned spike trains; see Methods) in both structures. As suggested by the previous examples, pairwise coupling among LMN-HD cells was less related to angular offset than in the ADN (Figure 1G–H; Supp. Figure 2D-E). This was further supported by cross-correlograms showing that LMN-HD cell pairs with opposite tuning tended to co-fire during non-REM (Figure 1I), suggesting that LMN coordination is dominated by unstructured, synchronous activity during this state. Nevertheless, regressing out population activity revealed that some level of tuning-related coordination was preserved in LMN-HD cell pairs (Figure 1J).

Could the reduced structure in LMN during non-REM reflect a diminished ability to influence downstream ADN neurons? To address this, we measured LMN-ADN cross-correlograms at short time scales. These revealed strong, positively biased interactions from LMN to ADN consistent with synaptic transmission during both wakefulness and sleep (Figure 1K, Supp Figure 2F-G), suggesting that LMN maintains its capacity to drive ADN spiking. However, the ability of LMN-HD population activity to predict ADN-HD population activity was markedly reduced during sleep compared to wakefulness (Figure 1L), indicating a functional decoupling between the two structures.

Together, these observations argue against the presence of a stable attractor in the LMN during non-REM sleep and suggest instead that the ADN-HD population maintains coherent dynamics independently of its upstream input.

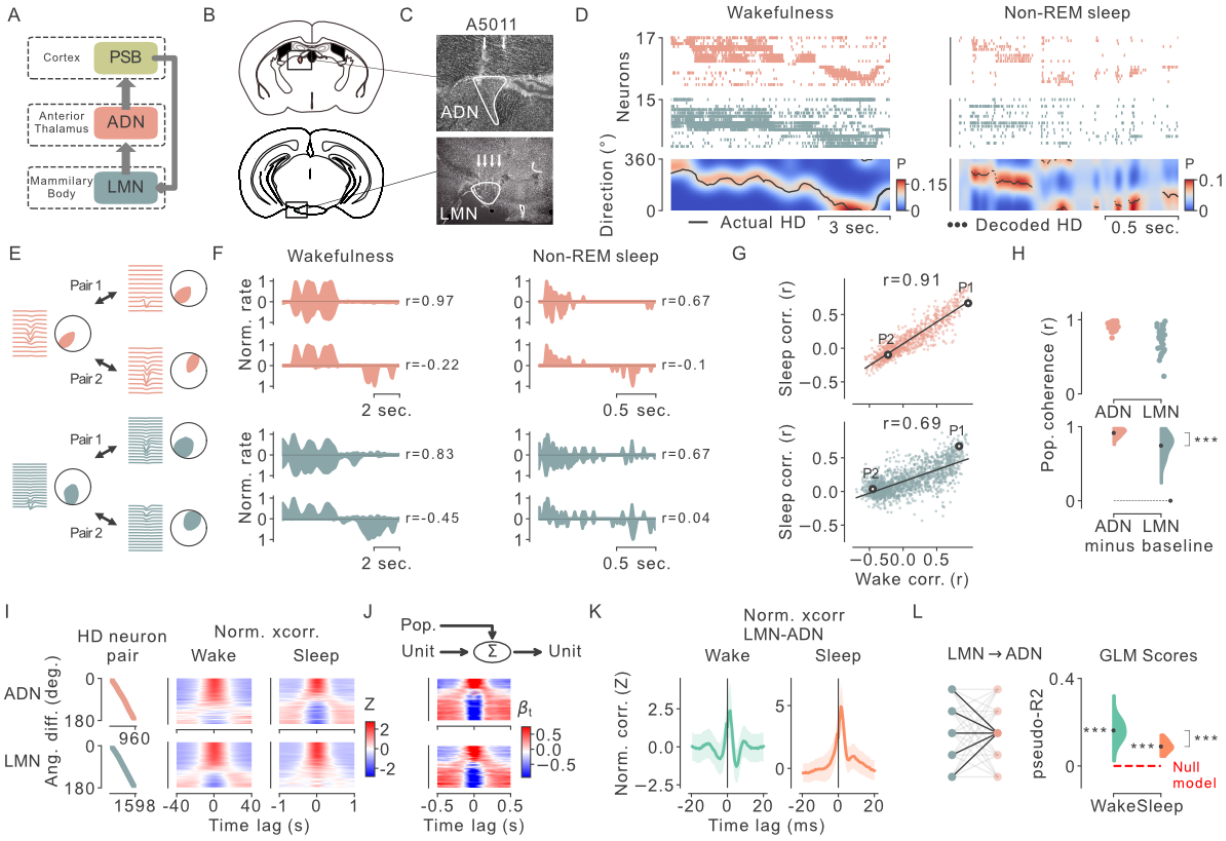

Figure 1 | Decreased population coherence in LMN, but not ADN, during non-REM.

(A) Schematic of the head-direction circuit involving the cortex (postsubiculum, PSB), anterodorsal nucleus of the thalamus (ADN), and lateral mammillary nucleus (LMN).

(B) Coronal diagrams showing silicon probe tracks targeting the LMN (bottom) and ADN (top).

(C) Histological verification of probe locations (arrows) in the ADN (top) and LMN (bottom).

(D) Top: Raster plots of HD cell spiking activity in ADN (orange) and LMN (blue) during wakefulness (left) and non-REM sleep (right). Bottom: Decoded head-direction signal, showing clear activity packets during wakefulness in both structures (left), but preserved only in ADN during non-REM (right). Black line indicates actual HD during wakefulness, and decoded HD signal during sleep (see Methods) .

(E) Tuning curves and waveforms of three example HD cells in the ADN (top) and LMN (bottom).

(F) Normalized firing rate and correlation coefficients (*r*) for representative HD cell pairs in ADN (top) and LMN (bottom), during wakefulness (left) and non-REM sleep (right).

(G) Correlation of pairwise coupling during wake and sleep for all HD cell pairs in ADN (top) and LMN (bottom). Circled points indicate selected example pairs shown in (E,F).

(H) Population coherence during non-REM, quantified as pairwise coupling minus a spike-shuffled baseline, was significantly higher in ADN compared to LMN (Mann–Whitney; U=111; $p<0.001$; $n_{ADN}=24$; $n_{LMN}=35$ sessions).

(I) Left: Distribution of angular differences between preferred directions of HD neuron pairs in ADN and LMN. Middle: Normalized cross-correlograms for pairs sorted by angular difference during wake and sleep. LMN-HD cells show aberrant co-firing across the full tuning range during sleep.

(J) Left: Method for regressing out population coupling to isolate pairwise interactions. Right: Residual coupling (β_t) remains directionally specific in ADN and partially preserved in LMN.

(K) Normalized cross-correlograms of LMN→ADN cell pairs during wakefulness (green) and non-REM sleep (orange) show strong short-latency peaks consistent with monosynaptic influence in both states.

(L) Generalized linear model (GLM) fits show that LMN-HD population activity predicts ADN spiking better during wake than sleep (pseudo-R^2. Mann-Whitney U test; U=67; $p<0.001$ across conditions; n=26 sessions). GLM models were still significantly better than predicting mean firing rate for both wake and sleep (Wilcoxon signed-rank test; $p<0.001$).

During non-REM sleep, the coherence of LMN population activity depends on cortical feedback.

The decrease—but not complete abolition—of LMN-HD cell population coherence during non-REM could reflect intrinsic attractor-like properties of the LMN circuit and its inputs from the brainstem [12,30,31,33]. Alternatively, this residual coordination may arise from cortical feedback, notably from the postsubiculum (PSB) [37,38]. To test this possibility, we implanted $n = 4$ mice with probes targeting both the LMN and PSB (Supp. Figure 3A-B). As in LMN-ADN dual recordings, LMN-HD cells exhibited bouts of unstructured activity during non-REM, while PSB maintained a well-defined activity packet (Figure 2A). Cross-correlograms between spike trains in the two

142 regions showed peaks at short time scales consistent with cortico-mammillary synaptic
143 transmission (Figure 2B).

144 During non-REM sleep, thalamocortical networks display activity levels comparable to
145 wakefulness during "UP" states, interrupted by brief periods of global silencing known as
146 "DOWN" states (Steriade et al. 1993). Crucially, LMN population coherence was decreased
147 during cortical DOWN states (Figure 2A, E), indicating that PSB feedback may be necessary to
148 organize LMN-HD activity.

149 To directly test the role of cortical feedback, we silenced PSB activity by transfecting local
150 inhibitory neurons (using VGAT-Cre mice) with the red-light–activated depolarizing opsin
151 Chrimson (see Methods; [40]). Red-light illumination of PSB led to robust, global suppression of
152 PSB activity (Figure 2F, Supp. Figure 4A-D). Next, we injected Chrimson in the PSB of VGAT-
153 Cre mice (n = 7 mice) and implanted probes in the ipsilateral LMN (Supp. Figure 5),
154 consistent with the lateralized nature of the PSB→LMN projection [41–43].

155 During wakefulness, silencing PSB did not significantly affect LMN firing rates or population
156 coherence (Figure 2G–I). However, tuning curves of LMN-HD cells became slightly broader
157 (Figure 2J), consistent with a role for PSB feedback in anchoring the internal HD signal to
158 environmental cues [35,41].

159 By contrast, silencing PSB during non-REM induced profound changes in LMN population
160 activity. LMN firing rates dropped to approximately half of their baseline levels (Figure 2K–L),
161 and—critically—population coherence became indistinguishable from random spiking (Figure
162 2M-N).

Together, these results reveal a crucial role for cortical feedback in organizing coherent population dynamics in the LMN-HD system during non-REM sleep.

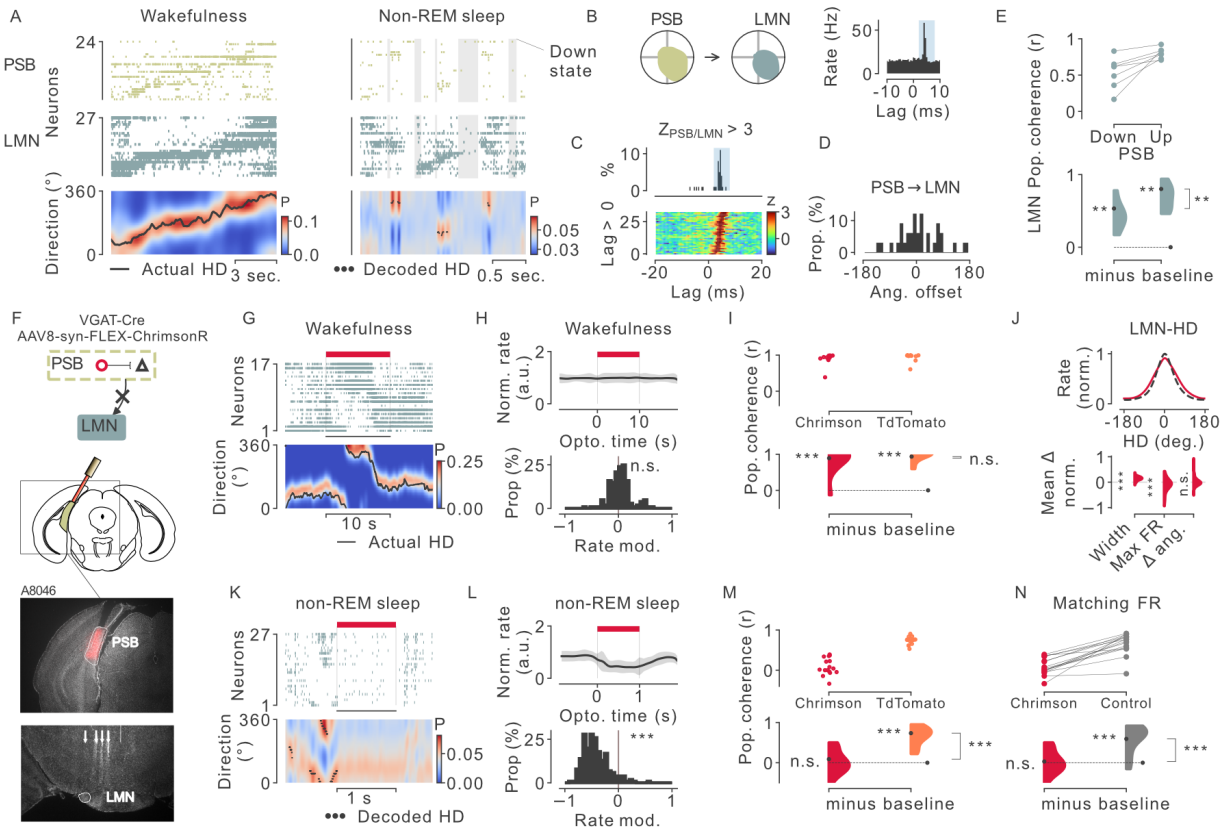

Figure 2 | Cortical feedback organizes LMN-HD cell activity during non-REM sleep.

(A) Simultaneous recordings of HD cells in PSB (yellow) and LMN (blue) during wakefulness (left) and non-REM sleep (right). Top: spike rasters. Bottom: actual (wake) or decoded (sleep) head direction. Activity packets persist in PSB across states but are disrupted in LMN during non-REM.

(B) Left; tuning curve of two HD cells recorded simultaneously in the PSB and LMN. Right, cross-correlograms of the two cells spike trains showing a significant peak at short (4 ms) timelag.

(C) Color-coded cross-correlograms (bottom) for all significantly coupled PSB→LMN pairs (Z > 3) and distribution of peak timelags (top).

(D) Distribution of angular tuning offsets for PSB→LMN cell pairs, indicating broad directional convergence.

(E) Top: LMN population coherence during cortical DOWN vs. UP states. Bottom: LMN coordination was larger during UP states compared to DOWN states, as measured by baseline-subtracted pairwise correlation (Wilcoxon-signed rank test; W=28; $p<0.01$; n=7 sessions). In both conditions, LMN coordination was larger than shuffle (Wilcoxon-signed rank test; W=28; $p<0.01$)

(F) Top: Experimental design. VGAT-Cre mice received Cre-dependent Chrimson injections in PSB and were implanted with LMN probes. Bottom: Histological verification of PSB infection and fiber location.

(G) Example wake session with PSB silencing (red bar). Top: LMN spike raster. Bottom: decoded HD signal remains coherent.

(H) Top: Normalized LMN firing rate during PSB silencing in wakefulness. Bottom: Distribution of modulation indices shows no significant change (Wilcoxon-signed; W=4465; p=0.10; n=145 neurons).

(I) LMN population coherence during wake in Chrimson (red) and control (TdTomato, orange) mice. No significant difference across conditions (Mann-Whitney; U=188; p=0.22; $n_{Chrimson}$=24; $n_{TdTomato}$=20), and coherence remained higher than chance in both ($U_{Chrimson}$=572; $p < 0.001$; $U_{TdTomato}$=400; $p<0.001$).

(J) Top, Average centered LMN-HD cell tuning curves during control periods (dashed line) and PSB silencing (red). Bottom, Change in tuning curve properties (width, peak firing rate, and preferred direction) during PSB silencing in wakefulness (Wilcoxon-signed; W_{Widths}=107; $p<0.001$; $W_{Max\ FR}$=1376; $p<0.001$; $W_{\Delta Ang}$=4187; p=0.19).

(K) Same as (G) during a non-REM sleep session.

(L) Top: Change in mean LMN firing rate during PSB silencing in non-REM. Bottom: Distribution of modulation indices (Wilcoxon-signed; W=349; $p<0.001$; n=204 neurons).

(M) Change in LMN population coherence during non-REM when PSB is silenced, but not in controls (Mann-Whitney; U=11; $p<0.001$; $n_{Chrimson}$=16; $n_{TdTomato}$=15). Coherence is not different from random baseline with Chrimson (Mann-Whitney; U=136; p=0.38) and remain higher with TdTomato (Mann-Whitney; U=225; $p<0.001$)

(N) Difference in coherence after matching LMN firing rates between Chrimson and control mice, confirming effect is not due to firing rate alone (Mann-Whitney; U_{across}=28, $p < 0.001$; $U_{Chrimson}$=136; p=0.38; $U_{TdTomato}$=236; $p<0.001$; n=16 sessions).

210 **A coherent HD signal is generated in the ADN during non-REM**

211 The previous findings suggest that the ADN–PSB network can sustain structured population
212 activity even when its upstream input from the LMN becomes disorganized during non-REM.
213 However, since the PSB projects back to the thalamus both directly and indirectly [44,45], it remains
214 possible that the ADN still depends on cortical feedback to maintain a coherent HD signal.
215 Alternatively, coherent dynamics may arise intrinsically within the thalamus itself.

216 To test this, we repeated the PSB silencing experiment during sleep while recording from the
217 ADN-HD cell population (*n* =7 mice; Figure 3A–B; Supp Figure 6). Unilateral silencing of the
218 PSB led to a ~30% reduction in ADn firing rate (Figure 3C–D), likely reflecting the loss of
219 excitatory input from the ipsilateral LMN. Strikingly, however, the ADN-HD population
220 maintained internal coherence at levels indistinguishable from controls (Figure 3C, E). This
221 resilience may reflect the fact that, unlike the ipsilateral PSB→LMN projection, the ADN
222 receives input from both left and right LMN [12]. To further probe this hypothesis, we performed
223 bilateral PSB silencing. In this condition, ADN-HD firing dropped to approximately 56% of
224 baseline levels (Figure 3F–G). Yet even under this strong reduction in excitatory drive, the ADN-
225 HD population remained internally coherent (Figure 3H). We observed no significant differences
226 in ADN population coherence when silencing PSB during wakefulness (Supp Figure 7 A-F).

227 Together, these results indicate that coherent HD dynamics can emerge locally within the anterior
228 thalamus during non-REM sleep, independently of structured cortical or subcortical input.

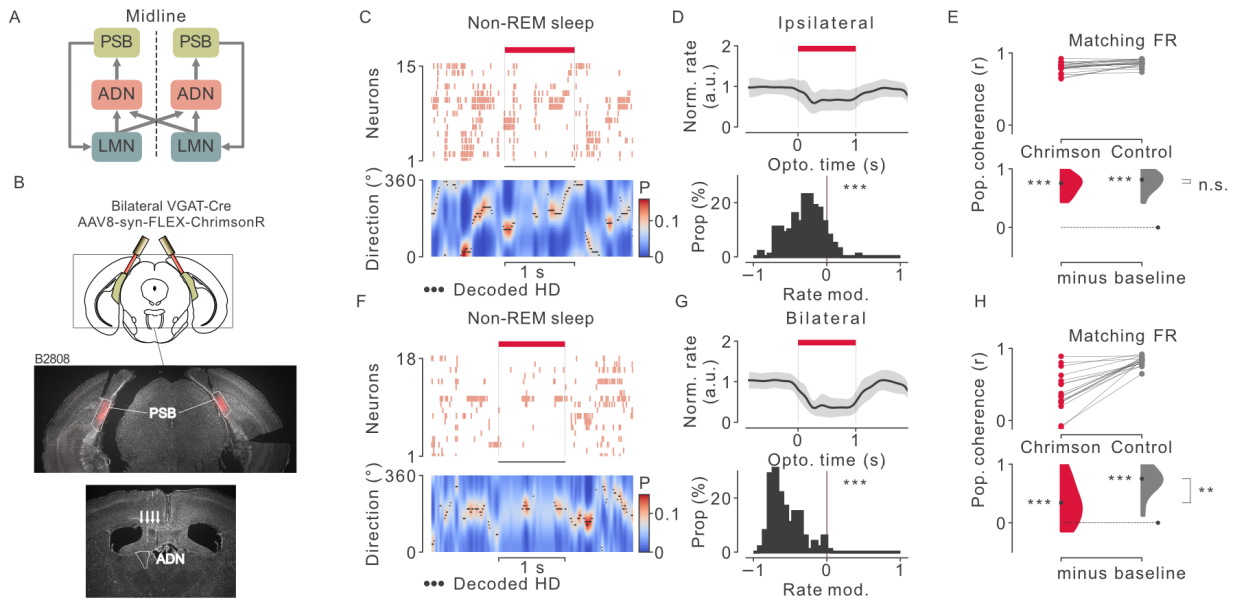

Figure 3 | ADN-HD cells maintain coherent population activity during cortical silencing.

(**A**) Schematic of bilateral HD system architecture. Each ADN receives input from both the ipsilateral PSB and the contralateral LMN.

(**B**) Experimental design. Top : VGAT-Cre mice received Cre-dependent Chrimson injections in PSB in either single hemisphere (Ipsilateral) or both hemisphere (Bilateral) and were implanted with probes targeting ADN. Bottom: Histological verification of PSB infection and fiber location for bilateral injections and ADN targeting.

(**C**) Example of ADN-HD population activity during non-REM sleep with unilateral PSB silencing (red bar). Top: spike raster. Bottom: decoded head direction.

(**D**) Top: Normalized ADN firing rate drops by ~30% during unilateral PSB silencing. Bottom: Histogram of modulation indices confirms a significant decrease (Wilcoxon-signed; W=492; $p < 0.001$; n=186 neurons).

(**E**) ADN-HD population coherence remains unchanged compared to controls despite firing rate reduction. Top: data matched for firing rate (FR). Bottom: baseline-subtracted coherence (Mann-Whitney; U_{Across}=143; p=0.28; U=361; $p < 0.001$ for both conditions compared to baseline).

(**F-H**) Same as (C-D), for bilateral PSB silencing. (Firing rate change: Wilcoxon-signed; W=6; $p < 0.001$; n=170 neurons; ~56% decrease. Coherence: U_{Across}=50; p<0.01; $U_{Chrimson}$=240; $p < 0.001$; $U_{Control}$=286; p<0.001).

A coherent HD signal emerges in the ADN from strongly non-linear filtering of LMN inputs.

Mechanistic models of attractor networks typically rely on strong local excitation combined with broad inhibitory connectivity, forming a structure akin to a passband filter in feature space that supports the emergence of a coherent activity packet [31,46]. However, thalamocortical relay cells lack local excitatory collaterals [47]. Instead, they interact primarily via shared connections to inhibitory neurons in the thalamic reticular nucleus (TRN) [36,44,48]. It is unclear how thalamic circuitry could support the emergence of structured activity.

Building on previous work, we observed that ADN-HD cells do not fire in a smooth, graded manner as the head moves through their tuning field. Rather, they show abrupt transitions from a low-firing "ground state" to a high-firing "activated state" (Figure 4A–B) [49]. This non-linearity was reflected in the interspike interval distributions, which were more bimodally distributed in ADN-HD cells compared to LMN-HD cells (Figure 4C).

Could such strong non-linearity be sufficient to explain the generative dynamics observed in the ADN? To address this, we simulated a simplified circuit comprising the three principal stages of the HD system studied here—LMN, ADN, and PSB—connected unilaterally in a closed loop (Figure 4D, Supp Figure 8A-B). The model incorporated three key features: (i) the LMN→ADN projection is divergent, with each LMN neuron contacting multiple ADN targets (as the number of neurons in the ADN is greater than in the LMN); (ii) the ADN is reciprocally connected with a local inhibitory population; and (iii) ADN neurons exhibit strong input–output non-linearity.

In the closed-loop configuration, with LMN neurons driven by noise and feedback from PSB to LMN intact, the circuit spontaneously generated a coherent activity packet (Figure 4E). As expected, when the loop was opened (i.e., PSB→LMN feedback removed), LMN activity remained unstructured. Remarkably, however, the ADN-HD population still exhibited significantly greater structure than predicted by chance (Figure 4F, Supp Figure 8 C). These simulations support the idea that structured HD dynamics can emerge in the anterior thalamus from random input, provided sufficient non-linearity and inhibitory shaping within the circuit.

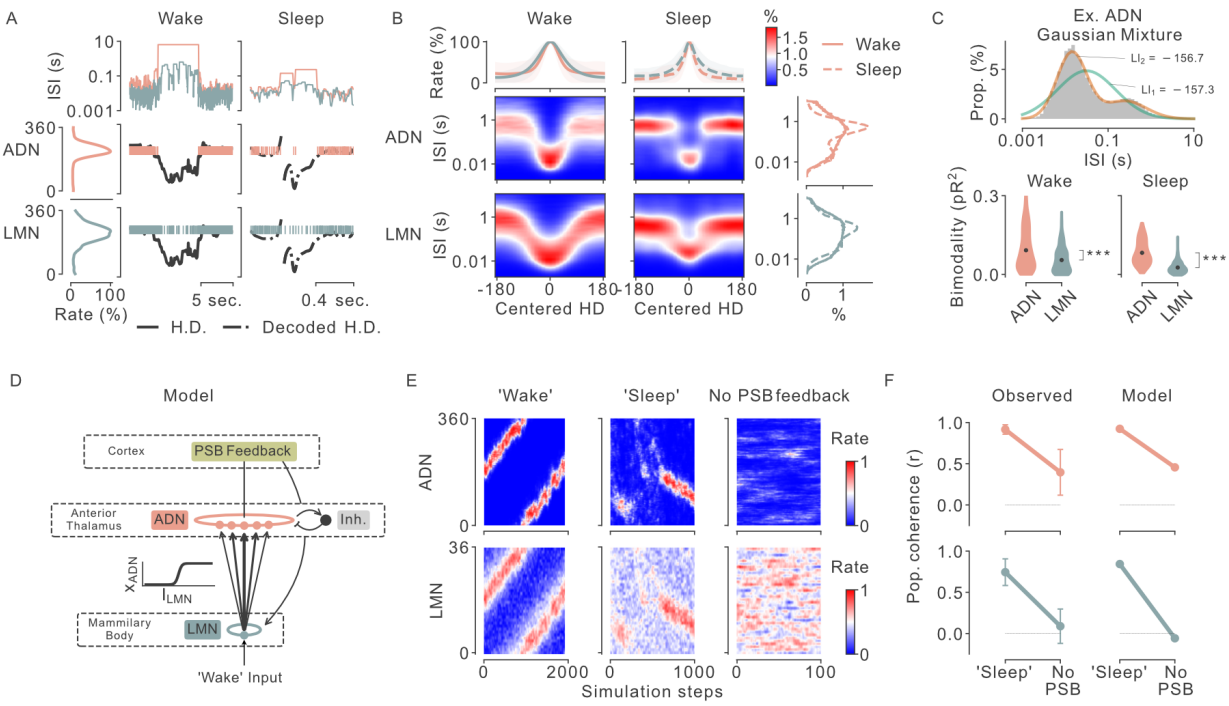

Figure 4 | Strong non-linear responses are sufficient to account for the generative properties of the ADN-HD cell population.

(**A**) Example activity of ADN and LMN-HD cells during wake and non-REM sleep. Left: interspike interval (ISI) distributions. Middle: head direction (black) and firing activity (colored) showing transitions between silent and active states. Right: decoded HD signal during non-REM.

(**B**) Average firing rate (top) and ISI distributions (middle) as a function of centered HD angle, aligned to each cell's preferred direction, for ADN (top row) and LMN (bottom row) during wake (left) and sleep (right). Right: marginal ISI distributions.

(**C**) Example ADN-HD cell fit with a two-component Gaussian mixture model, indicating bimodality. Bottom: quantification of bimodality index (pseudo-R^2) across cells in ADN and LMN during wake (Mann-Whitney; $U=57232$; $p<0.001$) and sleep ($U=78931$; $p < 0.001$).

(**D**) Schematic of the computational model incorporating LMN→ADN divergence, ADN inhibition, and PSB feedback. ADN neurons exhibit threshold-like nonlinear responses.

(**E**) Population activity of simulated HD cells in ADN (top) and LMN (bottom) under three conditions: 'Wake'-like input, 'Sleep'-like input (i.e. random inputs), and PSB silencing during 'sleep' ('Opto.').

(**F**) Population coherence values from real data (left) and the model (right), comparing sleep and optogenetic PSB silencing, for ADN (top) and LMN (bottom).

DISCUSSION

In this study, we performed multi-site electrophysiological recordings and optogenetic manipulations *in vivo* to reveal how the thalamus supports coherent population activity. Here, we show that during non-REM sleep, the pairwise correlation of LMN-HD cells is lower than during wakefulness, unlike ADN-HD cells. Transient inactivation of cortical feedback from the PSB with optogenetics led to a total decorrelation of LMN-HD cells, while maintaining coherent dynamics of ADN-HD cells. This indicated that thalamic circuits are capable of generating a coherent HD signal.

The data and simulations support the view that coherence in the ADN can emerge *de novo* from noise, provided the circuit architecture includes divergent input, local inhibitory interactions, and sharp non-linear response thresholds. This mechanism is particularly compelling in the thalamus,

where recurrent excitation is anatomically absent, and suggests a more active, generative role for thalamic nuclei than traditionally assumed.

The generation of the HD signal during wakefulness is thought to rely on reciprocal interactions between the dorsolateral tegmentum and the LMN [11,12,32,50,50]. Our findings suggest that this circuit becomes inoperative during non-REM sleep, with the weak coordination observed among LMN neurons instead being driven by cortical feedback. Notably, the structured activity of the LMN re-emerges during REM sleep, pointing to a state-dependent gating of internal dynamics. Neuromodulatory changes—particularly in cholinergic tone—may play a central role in this transition [15,51].

In our model, coordinated activity among ADN-HD neurons requires local inhibitory regulation. This inhibition can originate from the TRN, which is reciprocally connected with most thalamic nuclei (Jones 2005), including ADN [36,44,48]. Whether TRN neurons provide only broad, non-specific inhibition or contribute more selectively to the organization of HD activity—potentially through structured interactions among TRN neurons themselves—remains an open question.

The spontaneous and structured activity of HD cells during sleep is thought to coordinate activity in downstream structures such as the medial entorhinal cortex [52–54] and the hippocampus [55], and may thereby contribute to memory consolidation and replay processes [28,56–58].

Altogether, these findings support the view that during non-REM sleep, thalamocortical networks disengage from external input and shift toward intrinsically generated population dynamics [59].

330 **MATERIALS AND METHODS**

331 *Animals*

332 All experiments were approved by the Animal Care Committee of the Montreal Neurological
333 Institute. Adult (>8 weeks old) male C57BL/6J and VGAT-IRES-Cre (homozygous and
334 heterozygous) mice were used. C57BL6/6J and homozygous VGAT-IRES-Cre animals were
335 obtained from Jackson Laboratories (000664 and 028862 respectively), while heterozygous
336 VGAT-IRES-Cre animals were bred by crossing homozygous VGAT-IRES-Cre males with
337 C57BL/6J females. Animals were given food and water *ad libidum* and kept under a 12hr
338 light/dark cycle.

339 *Silicon Probe Implantation*

340 Animals were anesthetized with isoflurane (5% at induction, 1-2% at maintenance, airflow 2 L
341 min^{-1}) and subsequently placed in a stereotaxic frame (Kopf Instruments). Animals were injected
342 subcutaneously with carprofen (20 mg kg^{-1} body weight) and kept on a heating pad for the entire
343 procedure. Eyes were covered with lubricant eye gel (Systane) before removing fur with Veet
344 hair removal cream. The skin was disinfected with 2% Chlorhexidine before applying 5%
345 lidocaine cream. Surgical instruments were sterilized with a Geminator 500 before opening the
346 skin with a surgical blade. A silver wire was inserted into the cerebellum to serve as a reference
347 and ground. All probes were mounted on a moveable microdrive. Three types of probes were
348 used according to the target region: long four-shank probes (Neuronexus Buzsaki32L) were used
349 to target LMN, short four-shank probes (Neuronexus Buzsaki32S) were used to target ADN, and
350 single-shank probes (Cambridge NeuroTech H5) were used to target PSB. A hole was drilled
351 into the skull above the target site large enough to accommodate the size of the probe. Four-
352 shank probes were implanted perpendicular to the midline. Probes were slowly lowered above
353 the target site and secured to the skull using a light-cure adhesive (Kerr OptiBond) and dental

354 acrylic cement (Unifast Trad). A copper mesh was attached with a flowable composite
355 (FusionFlo) around the probe to reduce electrical noise in the recordings. Following the implant,
356 Animals were injected subcutaneously with saline (1 mL) and carprofen (20 mg kg^{-1}) and placed
357 on a heating pad until normal behaviour resumed. Carprofen injections were delivered every 24
358 hours for 72 hours after implantation. All animals were housed individually following the implant
359 surgery and allowed to recover for at least one week before electrophysiological recordings.
360 Silicon probe implantation coordinates were as follows: LMN implant AP (from Bregma): -2.23,
361 ML (from superior sagittal sinus): -0.75, DV (from dura): -4.90; ADN implant AP (from
362 Bregma): -0.4, ML (from superior sagittal sinus): -0.72, DV (from dura): -2.32; PSB implant AP
363 (from Lambda): +0.30, ML (from superior sagittal sinus): -2.35, DV (from dura): -1.00.
364 *Optogenetic experiments*
365 Animals were injected with either the viral vector AAV8-Syn-Flex-ChrimsonR-tdT (UNC; batch
366 number AV5844D) or AAV8-CAG-Flex-tdTomato (UNC; batch number AV4912b), with
367 concentrations of $3.9x10^{12}$ and $5.5x10^{12}$ respectively. Viruses were subdivided into aliquots and
368 stored at -80 °C until use.
369 Animals were anesthetized using isoflurane and placed on the stereotaxic frame as previously
370 described. After exposing the skull, a small hole was drilled over the target site. Viruses were
371 injected at a speed of 50 nl min^{-1} for a total volume of 100 nL into the target site using a Nanofil
372 syringe (WPI) and a Pump 11 Elite Nanomite Programmable Syringe Pump (Harvard Apparatus)
373 mounted on the stereotaxic frame. Following injection, the needle was left in place for 10 minutes
374 to allow for proper diffusion and absorption of the virus before being slowly removed from the
375 brain. Unilaterally injected animals were injected in the left hemisphere at a 30° angle towards
376 the midline with the following coordinates: AP (from lambda): +0.28 mm, ML (from superior
377 sagittal sinus): -1.21, DV (from dura): -2.20. Bilaterally injected animals were injected at a 28°

378 angle towards the midline with the following coordinates: AP (from lambda) +0.28, ML (from
379 superior sagittal sinus) ± 1.33, DV (from dura) -1.90.
380 Animals were sutured (Ethicon Perma-hand Silk) and injected subcutaneously with sterile saline
381 (1 mL) before being placed back in their home cage over a heating pad until normal behaviour
382 resumed (max 30 mins). Animals were subcutaneously injected with carprofen every 24 hours
383 for 72 hours following the procedure and were allowed a recovery period of at least 14 days
384 before the implantation surgery.
385 Optic fibers (Doric Lenses; MFC_200/240-0.22_27mm_RM2_FLT) were implanted unilaterally
386 (left hemisphere) at a 30° angle towards the midline with the following coordinates: AP (from
387 lambda) +0.30, ML (from superior sagittal sinus) -1.10, DV (from dura) -1.50. All unilaterally
388 implanted ADN animals were also implanted with tungsten wires targeting the pyramidal layer
389 of CA1. Optic fibers were implanted bilaterally at a 28° angle towards the midline with the
390 following coordinates: AP (from lambda) +0.28 or +0.52, ML (from superior sagittal sinus) ±
391 1.23, DV (from dura) -1.45. Fibers were secured to the skull using a combination of a flowable
392 composite (FusionFlo) and dental acrylic cement (Unifast Trad).
393 Light power output of optic fibers was measured before each implantation and an output curve
394 was calculated for each fiber. Light output was set to 15mW for each recording session and laser
395 light was delivered from a 638 nm fiber-coupled laser diode module (Doric Lenses), controlled
396 with a laser diode module driver (Doric Lenses), to the optic fiber implants via patch cords.
397 During sleep recordings, light pulses (1s) were delivered at 0.2 Hz for 5 mins, followed by 5
398 mins of no stimulation. This cycle was repeated four times for a total of 240 light pulses in a 45-
399 min recording session. During wake recordings, light pulses (10s) were delivered at 0.5 Hz for 5
400 mins, followed by 5 mins of no stimulation. This cycle was repeated four times for a total of 60
401 light pulses over a 45-min recording session.

402 *Recording procedure*

403 Animals were recorded during random foraging behaviour either in a square (80 cm width, 50
404 cm height) or a circular (85 cm diameter, 50 cm height) open field. Both recording chambers
405 consisted of a metal frame supporting a gray plastic platform with gray walls. A white rectangular
406 cue card served as a salient landmark in the circular environment, while the square environment
407 contained different rectangular cue cards on three walls. Sleep sessions were performed in the
408 home cage.

409 Neurophysiological signals were acquired continuously at 20 kHz on a 256-channel RHD USB
410 interface board (Intan Technologies) and captured with Intan RHX software (Intan
411 Technologies). Recording cables were tethered to a motorized electrical rotary joint (AERJ;
412 Doric Lenses). Probes were lowered into the target structure in small (~35 µm) increments. Data
413 collection began at least 2 hours after the last adjustment.

414 The animals' position and orientation were tracked in 3D using several infrared cameras (Flex
415 13; Optotrack) located above the enclosure and coupled to the Motive motion capture system
416 (Optitrack). Position and head orientation were sampled at 120 Hz and synchronized with the
417 electrophysiological recording via voltage pulses registered by the RHD USB interface board
418 (Intan Technologies). Tracking markers were attached to the headcap. Video recording was
419 captured by an overhead camera (Flex 13; Optitrack) placed close to the rotary joint.

420 *Tissue processing*

421 Following the termination of experiments, animals were deeply anesthetized using a sodium
422 pentobarbital solution injected intraperitoneally and perfused transcardially with a 0.9%
423 phosphate-buffered saline solution followed by 4% paraformaldehyde. Brains were extracted and
424 stored in 4% paraformaldehyde for 12-24 hours before being transferred to a 30% sucrose
425 solution until the brains sank (48-72 hours). Brains were subsequently frozen to -80 °C and

426 sectioned with a freezing microtome coronally in 40 μm slices. Sections were washed,
427 counterstained with DAPI and mounted on glass slides with ProlongGold fluorescence antifade
428 medium. Sections containing probe tracts, with the exception of optogenetic animals injected and
429 implanted in the PSB, were additionally incubated with a Cy3 anti-mouse secondary antibody
430 (1:200 dilution; Cedarlane, 715-165-150) to help visualize the electrode tract. A widefield
431 fluorescence microscope (Leica) was used to obtain images of sections and verify the tracks of
432 silicone probe shanks, optic fiber position and viral expression.

433 *Spike sorting and unit classification*

434 Spike sorting was performed semi-automatically using Kilosort 4.0 [60] followed by manual
435 curation using the software Klusters [61]. At this stage, clusters lacking a distinct waveform and a
436 clear refractory period in their autocorrelogram (0–1 ms bin) were labeled as noise. Cluster pairs
437 showing similar waveforms and a clear refractory dip in their cross-correlograms (0–1 ms bin)
438 were merged.

439 *Sleep State classification*

440 To perform sleep scoring, tungsten wires were inserted in the pyramidal layer of CA1 in 7
441 animals and sleep stages were determined according to time-resolved spectrograms of the CA1
442 and animals' movements. For the animals without CA1 wires, sleep scoring was performed by
443 detecting theta frequency in the local field potential and animal movement. In all cases, stages
444 were visually inspected and manually adjusted.

445 *HD tuning curves and selection*

446 HD tuning curves were computed by dividing the spike count histogram by the occupancy time
447 histogram, using 3° bins, and smoothing the result with a Gaussian kernel with a standard
448 deviation of 12°. For each cell, HD information was computed as :

449 $$I = \sum_{i=1..n} \lambda(\theta_i) \, log_2(\lambda(\theta_i) \, / \, \lambda) \, p(\theta_i)$$

where $\lambda(\theta_i)$ denotes the firing rate of the cell in the i-th angular bin, λ is the cell's overall average firing rate during exploration, and $p(\theta_i)$ represents the occupancy probability—that is, the normalized time spent facing direction θ_i. The resulting information rate (in bits per second) was then divided by the cell's mean firing rate to yield the information content (in bits per spike), providing a measure independent of firing rate.

HD cells were identified through a two-step selection process. First, cells with a mean firing rate greater than 1 Hz and HD information exceeding 0.1 were retained. In the second step, the exploration epoch was divided into two equal halves, and tuning curves were computed separately for each segment. A Rayleigh test for directional tuning was applied, and cells with a Rayleigh score above 50 and a p-value below 0.0001 were selected. Only cells that met these criteria in both sub-epochs were classified as HD cells.

Decoded Head-direction

Head-direction was decoded from spiking activity using a Bayesian approach implemented in the *pynapple* package [62,63]. For the decoding shown in Figures 1–3 and Supplementary Figure 7, spike counts were computed in 100 ms bins during wakefulness and 5 ms bins during non-REM sleep. Tuning curves were calculated over 24 angular bins spanning 0° to 360°. For sleep decoding, only angles decoded from a non-uniform probability distribution are shown. Non-uniformity was assessed at each time step by thresholding the probability distribution, retaining only those with a normalized entropy less than 0.12.

Population coherence

Population coherence was computed as the correlation between the correlation coefficients of pairs of simultaneously recorded neurons. Spike trains were binned using 100 ms windows for wakefulness and REM sleep, and 20 ms windows for non-REM sleep. The resulting spike count

473 vectors were convolved with a Gaussian kernel with a standard deviation equal to three times the
474 bin width. Baseline population coherence was obtained by shuffling neuron identities.

475 To match firing rates between conditions during optogenetic stimulation, we first computed the
476 change in firing rate between the stimulation epoch and the immediately preceding control epoch.
477 If the change was negative, spikes from the control epoch were randomly subsampled to match
478 the firing rate observed during stimulation. This subsampling procedure was repeated 1,000
479 times, and the Pearson correlation for each neuron pair was averaged across all samples.

480 *Cross-correlograms*

481 Cross-correlograms between pairs of neurons were computed using 100 ms bins for wakefulness
482 and 10 ms bins for non-REM sleep.

483 *Detection of monosynaptic connections*

484 Spike train cross-correlograms were computed over a ±100 ms window using 0.5 ms bins and
485 convolved with a Gaussian kernel (σ = 10 ms) to estimate the baseline firing rate. The raw cross-
486 correlograms were then z-scored relative to this baseline. A putative monosynaptic connection
487 was deemed significant if at least two consecutive bins within the 2–8 ms interval exceeded 3
488 standard deviations above the baseline.

489 *Generalized Linear Model*

490 Generalized Linear Models (GLMs) were implemented using the *Nemos* package
491 (https://nemos.readthedocs.io/en/latest/). All models were solved using the L-BFGS optimization
492 algorithm with Ridge (L2) regularization. A regularization coefficient of 0.001 was applied
493 uniformly across all model fits. GLM-based cross-correlograms were generated by binning spike
494 trains into 100 ms bins during wakefulness and 10 ms bins during non-REM sleep. The spike
495 train of neuron i was modeled as a Poisson process conditioned on the time-lagged activity of

neuron j and the population firing rate excluding neuron j. Temporal windows of 10 s (wakefulness) and 1 s (non-REM sleep) were used for defining the lagged inputs.

GLMs predicting ADN spiking activity from LMN inputs were fit using 10 ms-binned spike data for both wakefulness and non-REM sleep. Model performance was evaluated using the pseudo-R2 metric : $pR_2 = 1 - \frac{log\ L_{model}}{log\ L_{null}}$

Detection of Up and Down states

Down states were detected by pooling spikes from all PSB units. The combined spike trains were binned in 10 ms intervals and smoothed with a Gaussian kernel whose standard deviation was twice the bin size. Down states were identified by thresholding at the 50th percentile of the smoothed firing rate during non-REM sleep. Down epochs separated by less than 100 ms were merged, and epochs shorter than 20 ms or longer than 2 s were excluded. Up states were defined as the complement of down states during non-REM sleep.

Gaussian mixture of ISI distribution

Gaussian mixture models were fitted using the *scikit-learn* package. Only ISI values between 2 ms and 10 s were used to fit the Gaussian models. Bimodality was quantified using the pseudo-R^2 metric: $pR_2 = 1 - \frac{log\ L_{2\ Gaussian}}{log\ L_{1\ Gaussian}}$.

Network model

We implemented a recurrent neural network model comprising three interconnected populations representing the lateral mammillary nucleus (LMN), anterior dorsal thalamic nucleus (ADN), and thalamic reticular nucleus (TRN). The model was implemented in Python using NumPy and Numba for computational efficiency.

The network consisted of $N_{LMN} = 36$ units, $N_{ADN} = 360$ units and a single unit representing the TRN. All units were modeled as rate-based neurons with first-order dynamics governed by the differential equation:

$$\tau \frac{dx}{dt} = -x + I + noise$$

where x is the membrane potential variable, τ=0.1 is the integration time constant, I represents synaptic inputs and external drives, and noise is an additive Gaussian term modeling stochastic fluctuations.

LMN and TRN activity is governed by linear thresholding (rectified linear units) with $r_{LMN} = max(0, x_{LMN})$ and $r_{TRN} = max(0, x_{TRN})$, whereas ADN units used a sigmoidal transfer function:

$$r_{ADN} = \frac{1}{1 + exp^{(-\beta(x_{ADN} - \theta)}}$$

with slope parameter β=5 and threshold θ=1.

Independent Gaussian noise was injected into each population to capture intrinsic neuronal variability, with standard deviations parameterized as $\sigma_{LMN} = 1$, $\sigma_{ADN} = 1$ and $\sigma_{TRN} = 0.1$. During wakefulness, LMN units received a rotating external input, implemented as a periodically shifted Gaussian bump, mimicking a HD signal. A constant drive term $D_{LMN} = 1$ was added to LMN units to maintain baseline activation. An external input scaling parameter I_{LMN} controlled the strength of the external input drive, which was set to 1.0 during wakefulness and set to zero to simulate sleep.

Connections from LMN to ADN were arranged in a circular topology using Gaussian-weighted synaptic weights with standard deviation σ=100 (Supp. Figure 8). This circular connectivity ensured that ADN units received inputs preferentially from LMN units coding nearby directions on the ring.

The TRN unit received excitatory input from the summed activity of ADN neurons, scaled by $w_{ADN \rightarrow TRN} = 1.0$. In turn, the TRN inhibited ADN neurons through feedback weights scaled by $w_{TRN \rightarrow ADN} = 0.04$. This inhibitory feedback loop controlled the excitability of the ADN population and regulated its dynamics.

A feedback pathway from ADN to LMN was implemented to simulate the feedback from PSB. This connection used a circular weight matrix with narrower tuning (σ=10) compared to the LMN-to-ADN feedforward pathway. PSB feedback matrix was scaled by a factor $w_{PSB \rightarrow LMN} = 0.03$.

During "wakefulness", external input to LMN was enabled and feedback pathways were active. During "sleep", external input to LMN was suppressed. During "optogenetic", feedback weights from the ADN units back to the LMN units were artificially set to 0.

Data analysis and statistics

All analyses were done in python with the following libraries : Scipy, Numpy, Matplotlib, Scikit-Learn and Pynapple [63].

AUTHOR CONTRIBUTIONS

Conceptualization: GV, SSC, AP; Methodology: GV, SSC, AP; Software: GV, AP; Validation: GV, SSC, AP; Formal analysis: GV; Investigation: GV, SSC; Resources: AP; Data Curation:

GV, SSC; Writing - Original Draft: GV, SSC, AP; Writing - Review & Editing: GV, SSC, AP; Visualization: GV, SSC, AP; Supervision: AP; Project administration: AP; Funding acquisition: AP

ACKNOWLEDGMENTS

We would like to thank Lynda Mainville for technical support. We are thankful to the members of Peyrache laboratory for comments on the earlier version of the manuscript. This work was supported by a Canadian Research Chair in Systems Neuroscience (AP), CIHR Project Grant 180330 and 190289 (AP), NSERC Discovery Grant RGPIN-2018-04600 (AP), and Vanier CGS (SSC).

REFERENCES

1. Sherman, S. M. & Guillery, R. W. The role of the thalamus in the flow of information to the cortex. *Philos. Trans. R. Soc. Lond. B. Biol. Sci.* **357**, 1695–1708 (2002).
2. Saalmann, Y. B. & Kastner, S. Cognitive and Perceptual Functions of the Visual Thalamus. *Neuron* **71**, 209–223 (2011).
3. Wimmer, R. D. *et al.* Thalamic control of sensory selection in divided attention. *Nature* **526**, 705–709 (2015).
4. Crandall, S. R., Cruikshank, S. J. & Connors, B. W. A Corticothalamic Switch: Controlling the Thalamus with Dynamic Synapses. *Neuron* **86**, 768–782 (2015).
5. Rikhye, R. V., Gilra, A. & Halassa, M. M. Thalamic regulation of switching between cortical representations enables cognitive flexibility. *Nat. Neurosci.* **21**, 1753–1763 (2018).
6. Halassa, M. M. & Sherman, S. M. Thalamocortical Circuit Motifs: A General Framework. *Neuron* **103**, 762–770 (2019).
7. Guo, Z. V. *et al.* Maintenance of persistent activity in a frontal thalamocortical loop. *Nature* **545**, 181–186 (2017).
8. Phillips, J. M. *et al.* Primate thalamic nuclei select abstract rules and shape prefrontal dynamics. *Neuron* **113**, 2014-2027.e12 (2025).
9. Taube, J. S. Head direction cells recorded in the anterior thalamic nuclei of freely moving rats. *J. Neurosci.* **15**, 70–86 (1995).
10. Peyrache, A., Lacroix, M. M., Petersen, P. C. & Buzsáki, G. Internally organized mechanisms of the head direction sense. *Nat. Neurosci.* **18**, 569–575 (2015).
11. Taube, J. S. The Head Direction Signal: Origins and Sensory-Motor Integration. *Annu. Rev. Neurosci.* **30**, 181–207 (2007).
12. Sharp, P. E., Blair, H. T. & Cho, J. The anatomical and computational basis of the rat head-

direction cell signal. *Trends Neurosci.* **24**, 289–294 (2001).

13. Chaudhuri, R., Gerçek, B., Pandey, B., Peyrache, A. & Fiete, I. The intrinsic attractor manifold and population dynamics of a canonical cognitive circuit across waking and sleep. *Nat. Neurosci.* **22**, 1512–1520 (2019).
14. Senzai, Y. & Scanziani, M. A cognitive process occurring during sleep is revealed by rapid eye movements. *Science* **377**, 999–1004 (2022).
15. Hobson, J. A. & Pace-Schott, E. F. The cognitive neuroscience of sleep: neuronal systems, consciousness and learning. *Nat. Rev. Neurosci.* **3**, 679–693 (2002).
16. Moruzzi, G. & Magoun, H. W. Brain stem reticular formation and activation of the EEG. *Electroencephalogr. Clin. Neurophysiol.* **1**, 455–473 (1949).
17. Steriade, M., McCormick, D. A. & Sejnowski, T. J. Thalamocortical Oscillations in the Sleeping and Aroused Brain. *Science* **262**, 679–685 (1993).
18. Harris, K. D. & Thiele, A. Cortical state and attention. *Nat. Rev. Neurosci.* **12**, 509–523 (2011).
19. Buzsáki, G. & Draguhn, A. Neuronal Oscillations in Cortical Networks. *Science* **304**, 1926–1929 (2004).
20. Stringer, C., Pachitariu, M., Steinmetz, N., Carandini, M. & Harris, K. D. High-dimensional geometry of population responses in visual cortex. *Nature* **571**, 361–365 (2019).
21. Luczak, A., Barthó, P. & Harris, K. D. Spontaneous Events Outline the Realm of Possible Sensory Responses in Neocortical Populations. *Neuron* **62**, 413–425 (2009).
22. Manley, J. *et al.* Simultaneous, cortex-wide dynamics of up to 1 million neurons reveal unbounded scaling of dimensionality with neuron number. *Neuron* **112**, 1694-1709.e5 (2024).

23. Taube, J. S., Muller, R. U. & Ranck, J. B. Head-direction cells recorded from the postsubiculum in freely moving rats. I. Description and quantitative analysis. *J. Neurosci.* **10**, 420–435 (1990).
24. Peyrache, A., Duszkiewicz, A. J., Viejo, G. & Angeles-Duran, S. Thalamocortical processing of the head-direction sense. *Prog. Neurobiol.* **183**, 101693 (2019).
25. Winter, S. S., Clark, B. J. & Taube, J. S. Disruption of the head direction cell network impairs the parahippocampal grid cell signal. *Science* **347**, 870–874 (2015).
26. Harland, B. *et al.* Lesions of the Head Direction Cell System Increase Hippocampal Place Field Repetition. *Curr. Biol.* **27**, 2706-2712.e2 (2017).
27. Valerio, S. & Taube, J. S. Path integration: how the head direction signal maintains and corrects spatial orientation. *Nat. Neurosci.* **15**, 1445–1453 (2012).
28. Levenstein, D., Efremov, A., Eyono, R. H., Peyrache, A. & Richards, B. Sequential predictive learning is a unifying theory for hippocampal representation and replay. 2024.04.28.591528 Preprint at https://doi.org/10.1101/2024.04.28.591528 (2024).
29. Ajabi, Z., Keinath, A. T., Wei, X.-X. & Brandon, M. P. Population dynamics of head-direction neurons during drift and reorientation. *Nature* **615**, 892–899 (2023).
30. Redish, A. D., Elga, A. N. & Touretzky, D. S. A coupled attractor model of the rodent head direction system. *Netw. Comput. Neural Syst.* **7**, 671 (1996).
31. Zhang, K. Representation of spatial orientation by the intrinsic dynamics of the head-direction cell ensemble: a theory. *J. Neurosci.* **16**, 2112–2126 (1996).
32. Skaggs, W., Knierim, J., Kudrimoti, H. & McNaughton, B. A Model of the Neural Basis of the Rat' s Sense of Direction. in *Advances in Neural Information Processing Systems* vol. 7 (MIT Press, 1994).
33. McNaughton, B. L., Battaglia, F. P., Jensen, O., Moser, E. I. & Moser, M.-B. Path

integration and the neural basis of the ‘cognitive map’. *Nat. Rev. Neurosci.* **7**, 663–678 (2006).

34. Blair, H. T., Cho, J. & Sharp, P. E. Role of the Lateral Mammillary Nucleus in the Rat Head Direction Circuit: A Combined Single Unit Recording and Lesion Study. *Neuron* **21**, 1387–1397 (1998).
35. Goodridge, J. P., Dudchenko, P. A., Worboys, K. A., Golob, E. J. & Taube, J. S. Cue control and head direction cells. *Behav. Neurosci.* **112**, 749–761 (1998).
36. Duszkiewicz, A. J. *et al.* Local origin of excitatory–inhibitory tuning equivalence in a cortical network. *Nat. Neurosci.* **27**, 782–792 (2024).
37. Shibata, H. Descending projections to the mammillary nuclei in the rat, as studied by retrograde and anterograde transport of wheat germ agglutinin–horseradish peroxidase. *J. Comp. Neurol.* **285**, 436–452 (1989).
38. Yoder, R. M. & Taube, J. S. Projections to the anterodorsal thalamus and lateral mammillary nuclei arise from different cell populations within the postsubiculum: Implications for the control of head direction cells. *Hippocampus* **21**, 1062–1073 (2011).
39. Steriade, M., Nunez, A. & Amzica, F. A novel slow (< 1 Hz) oscillation of neocortical neurons in vivo: depolarizing and hyperpolarizing components. *J. Neurosci.* **13**, 3252–3265 (1993).
40. Klapoetke, N. C. *et al.* Independent optical excitation of distinct neural populations. *Nat. Methods* **11**, 338–346 (2014).
41. Yoder, R. M., Peck, J. R. & Taube, J. S. Visual Landmark Information Gains Control of the Head Direction Signal at the Lateral Mammillary Nuclei. *J. Neurosci.* **35**, 1354–1367 (2015).
42. Allen, G. V. & Hopkins, D. A. Mamillary body in the rat: Topography and synaptology of

projections from the subicular complex, prefrontal cortex, and midbrain tegmentum. *J. Comp. Neurol.* **286**, 311–336 (1989).

43. Gonzalo-Ruiz, A., Alonso, A., Sanz, J. M. & Llinás, R. R. Afferent projections to the mammillary complex of the rat, with special reference to those from surrounding hypothalamic regions. *J. Comp. Neurol.* **321**, 277–299 (1992).
44. Vantomme, G. *et al.* A Thalamic Reticular Circuit for Head Direction Cell Tuning and Spatial Navigation. *Cell Rep.* **31**, (2020).
45. van Groen, T. & Wyss, J. M. The postsubicular cortex in the rat: characterization of the fourth region of the subicular cortex and its connections. *Brain Res.* **529**, 165–177 (1990).
46. Amari, S. Dynamics of pattern formation in lateral-inhibition type neural fields. *Biol. Cybern.* **27**, 77–87 (1977).
47. Jones. *Thalamus*. (Cambridge University Press, Cambridge (GB), 2007).
48. Gonzalo-Ruiz, A. & Lieberman, A. R. Topographic organization of projections from the thalamic reticular nucleus to the anterior thalamic nuclei in the rat. *Brain Res. Bull.* **37**, 17–35 (1995).
49. Levenstein, D. *et al.* Distinct ground state and activated state modes of firing in forebrain neurons. 2021.09.20.461152 Preprint at https://doi.org/10.1101/2021.09.20.461152 (2022).
50. Song, P. & Wang, X.-J. Angular Path Integration by Moving “Hill of Activity”: A Spiking Neuron Model without Recurrent Excitation of the Head-Direction System. *J. Neurosci.* **25**, 1002–1014 (2005).
51. Jones, B. Arousal and sleep circuits. *Neuropsychopharmacology* **45**, 6–20 (2020).
52. Vite, G. R., Ding, M. & Peyrache, A. Coherent thalamic inputs organize head direction signal in the medial entorhinal cortex. 2025.05.14.654107 Preprint at https://doi.org/10.1101/2025.05.14.654107 (2025).

53. Trettel, S. G., Trimper, J. B., Hwaun, E., Fiete, I. R. & Colgin, L. L. Grid cell co-activity patterns during sleep reflect spatial overlap of grid fields during active behaviors. *Nat. Neurosci.* **22**, 609–617 (2019).
54. Gardner, R. J., Lu, L., Wernle, T., Moser, M.-B. & Moser, E. I. Correlation structure of grid cells is preserved during sleep. *Nat. Neurosci.* **22**, 598–608 (2019).
55. Viejo, G. & Peyrache, A. Precise coupling of the thalamic head-direction system to hippocampal ripples. *Nat. Commun.* **11**, 2524 (2020).
56. Lee, A. K. & Wilson, M. A. Memory of Sequential Experience in the Hippocampus during Slow Wave Sleep. *Neuron* **36**, 1183–1194 (2002).
57. Wilson, M. A. & McNaughton, B. L. Reactivation of Hippocampal Ensemble Memories During Sleep. *Science* **265**, 676–679 (1994).
58. Peyrache, A. Querying hippocampal replay with subcortical inputs. *Curr. Opin. Neurobiol.* **77**, 102645 (2022).
59. Sejnowski, T. J. & Destexhe, A. Why do we sleep?1. *Brain Res.* **886**, 208–223 (2000).
60. Pachitariu, M., Sridhar, S., Pennington, J. & Stringer, C. Spike sorting with Kilosort4. *Nat. Methods* **21**, 914–921 (2024).
61. Hazan, L., Zugaro, M. & Buzsáki, G. Klusters, NeuroScope, NDManager: A free software suite for neurophysiological data processing and visualization. *J. Neurosci. Methods* **155**, 207–216 (2006).
62. Zhang, K., Ginzburg, I., McNaughton, B. L. & Sejnowski, T. J. Interpreting Neuronal Population Activity by Reconstruction: Unified Framework With Application to Hippocampal Place Cells. *J. Neurophysiol.* **79**, 1017–1044 (1998).
63. Viejo, G. *et al.* Pynapple, a toolbox for data analysis in neuroscience. *eLife* **12**, RP85786 (2023).

713 **SUPPLEMENTARY INFORMATION**

714 **Supplementary figures 1–8**

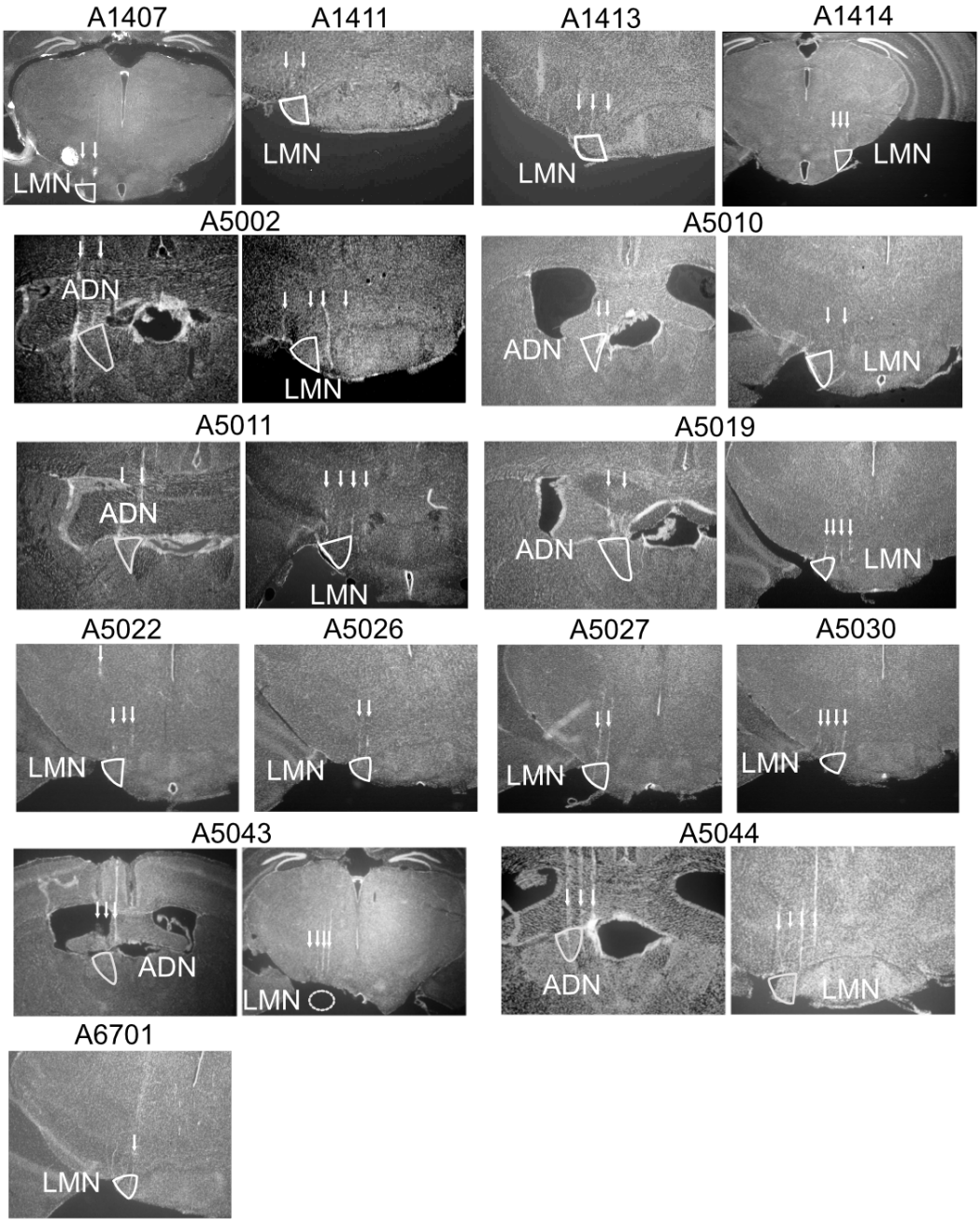

Supplementary figure 1 | Histological validation of electrode placement in the ADN and LMN.

Coronal histology showing silicon probe tracks (arrows) targeting the LMN and/or ADN for all animals presented in Figure 1.

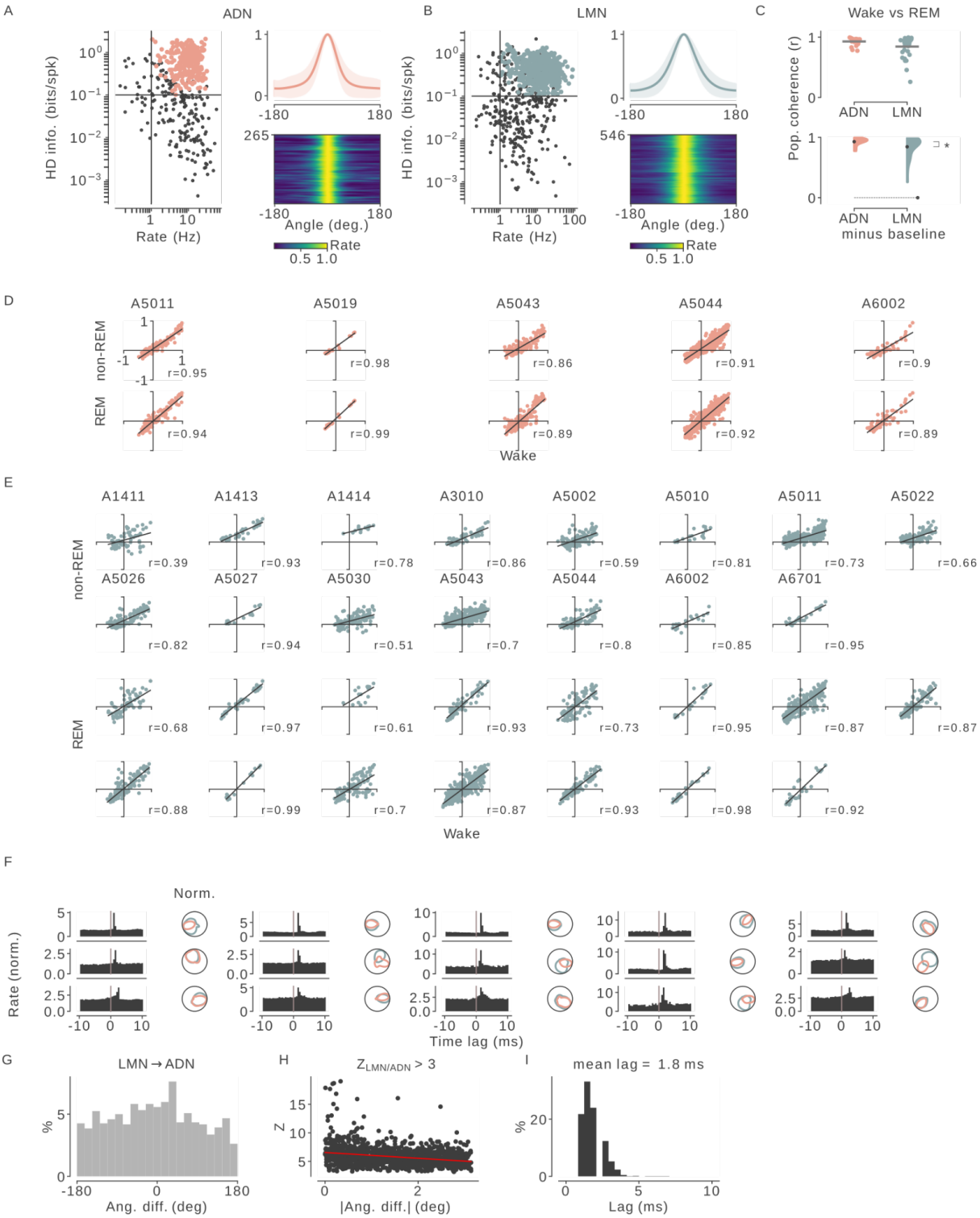

Supplementary Figure 2 | Population coherence of LMN and ADN units across individual sessions

(A) Left: Selection criteria for ADN units. Only cells with mean firing rates >1 Hz and HD information >0.1 bits/spike were included. Right: Tuning curves of all selected HD units in ADN.

(B) Same as (A), for LMN units.

(C) Population coherence during REM sleep for LMN and ADN units. Coherence was significantly higher in LMN (Mann–Whitney $U = 276$, $p = 0.026$; $n_{ADN} = 24$, $n_{LMN} = 35$).

(D) Population coherence of ADN units across wakefulness and non-REM sleep, shown per session.

(E) Same as (D), for LMN units.

(F) Representative LMN→ADN cross-correlograms showing significant peaks ($z > 3$) within the 1–8 ms range.

(G) Distribution of angular differences between preferred head directions of all significant LMN→ADN pairs.

(H) Peak z-scores between 1 and 8 ms for all significantly interacting pairs, plotted as a function of the absolute angular difference of their preferred directions.

(I) Distribution of time lags for all significantly interacting LMN→ADN pairs.

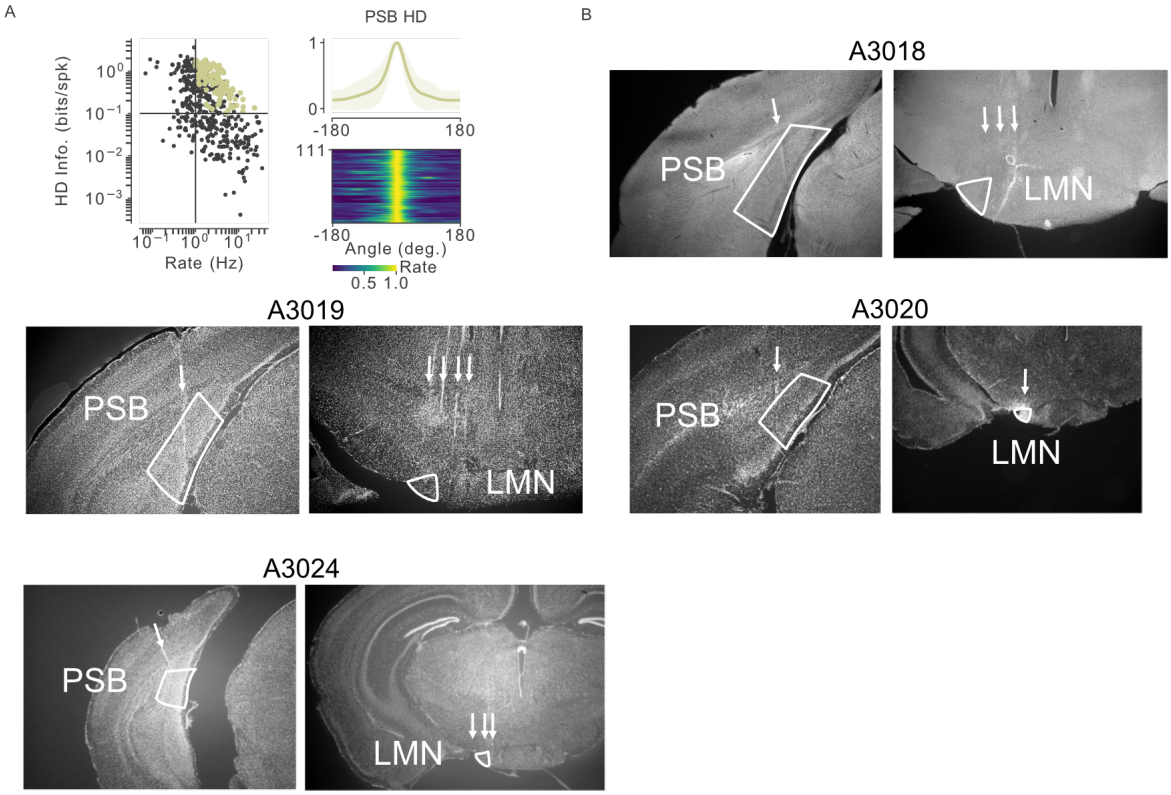

Supplementary figure 3 | PSB and LMN double recordings

(A) Left: PSB units selection. Only units with rate larger than 1 Hz and HD information larger than 0.1 bits/spk were selected. Right: Tuning curves for all HD-PSD units selected.

(B) Coronal histology showing silicon probe tracks (arrows) targeting the LMN and PSB.

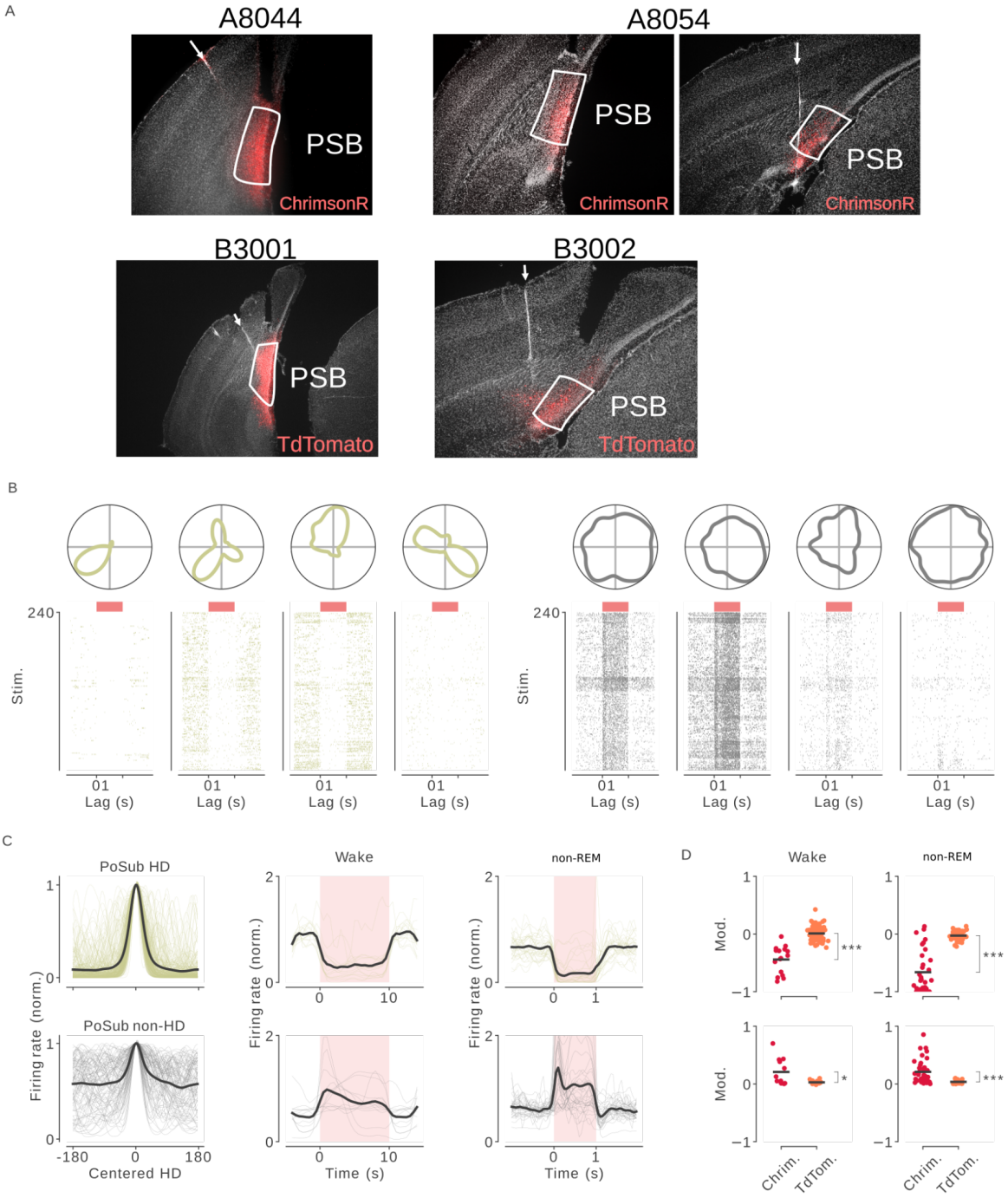

750

751 **Supplementary Figure 4 | PSB injections and recordings in VGAT-Cre mice**

752 **(A)** Coronal sections showing viral expression of ChrimsonR (n = 2 mice) or TdTomato (n = 2

753 mice) in the PSB, along with silicon probe placement. Arrows indicate probe tracks.

754 **(B)** Example tuning curves and spike rasters for four HD cells and four non-HD cells recorded

755 in the PSB during optogenetic stimulation in ChrimsonR-injected VGAT-Cre mice.

756 **(C)** Mean-centered tuning curves for HD cells (top) and non-HD cells (bottom) during

757 optogenetic stimulation.

(D) Mean firing rates of HD and non-HD cells during wakefulness and non-REM sleep, under optogenetic stimulation.

(E) Firing rate modulation in response to optogenetic stimulation, comparing ChrimsonR- and TdTomato-injected animals. For HD cells: Mann-Whitney; $U_{Wake}=36$; $p<0.001$; $U_{Sleep}=266$; $p<0.001$. For non-HD cells : Mann-Whitney; $U_{Wake}=195$; $p=0.02$; $U_{Sleep}=813$; $p<0.001$.

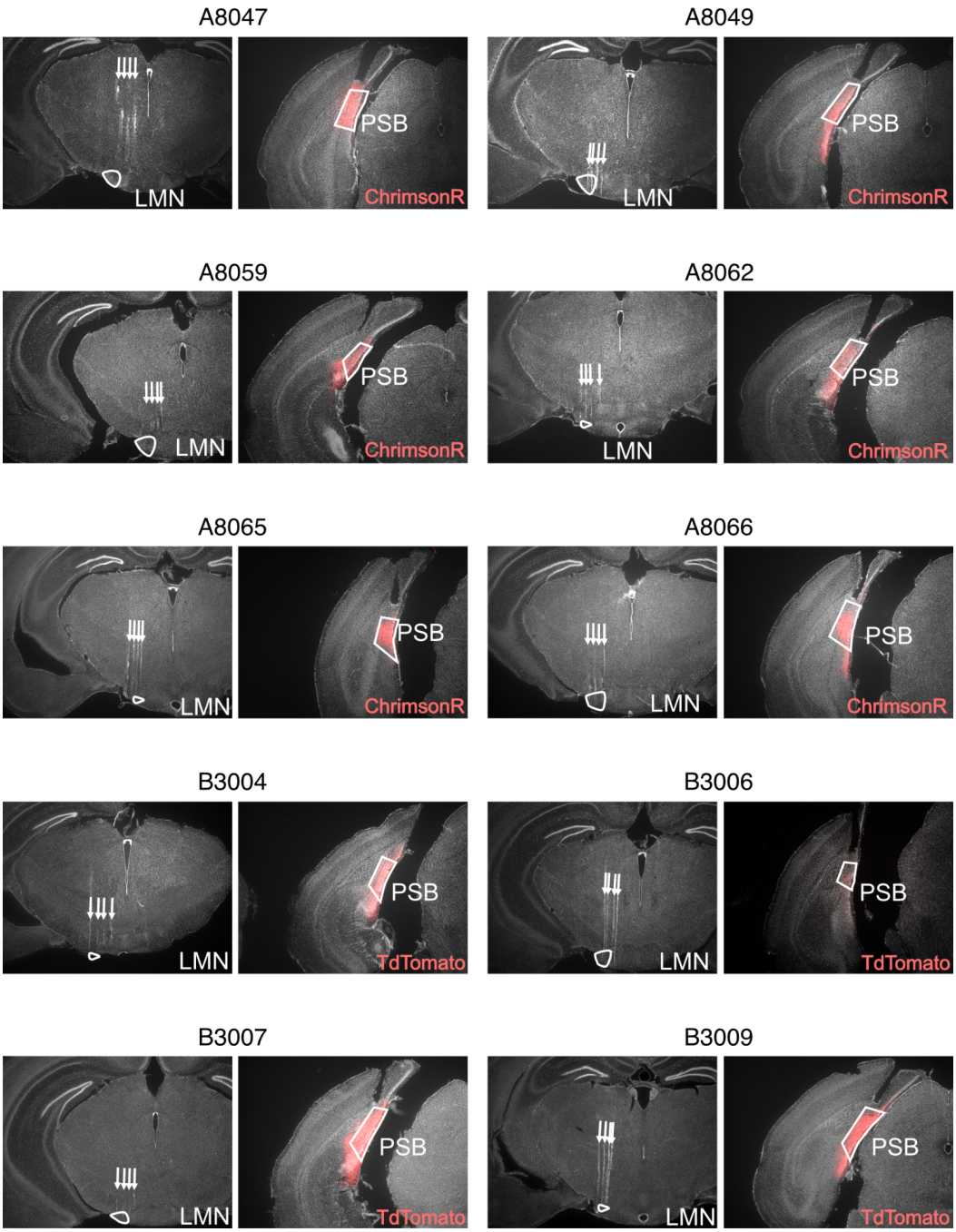

Supplementary Figure 5 | Histological verification of PSB injections and LMN recordings in VGAT-Cre mice

For each animal, coronal sections showing LMN (left) and PSB (right) histology are presented. Six mice were injected with ChrimsonR, and four control mice received TdTomato injections. Red labeling indicates the extent of viral expression.

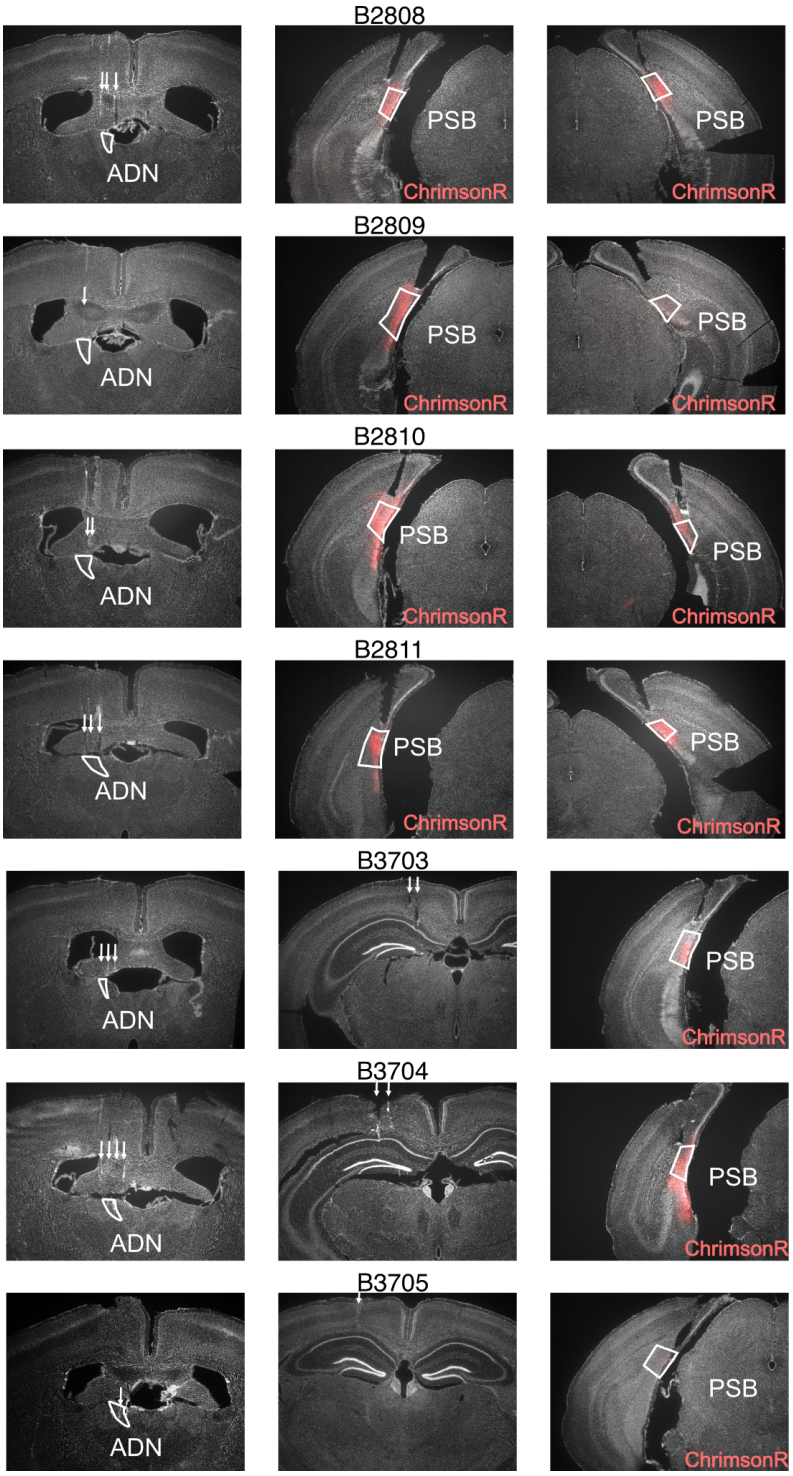

Supplementary Figure 6 | Histological verification of PSB injections and ADN recordings in VGAT-Cre mice

Red regions indicate viral expression. Mice B2809, B2810, and B2811 were injected bilaterally, while B3703, B3704, and B3705 received unilateral injections.

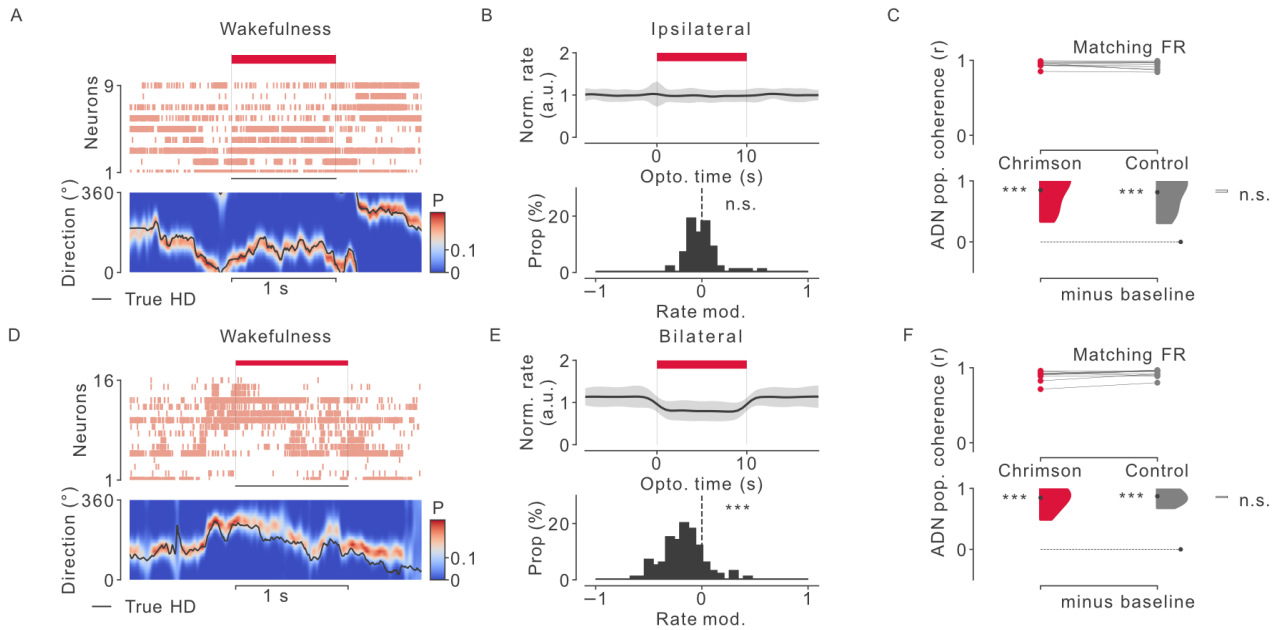

Supplementary figure 7 | Optogenetic stimulation of ADN during wakefulness

(**A**) Example of ADN-HD population activity during wakefulness with unilateral PSB silencing (red bar). Top: spike raster. Bottom: decoded head direction.

(**B**) Top: Normalized ADN firing rate during unilateral PSB silencing. Bottom: Histogram of modulation indices shows no decrease (Wilcoxon-signed; W=1082; $p = 0.07$; n=75 neurons).

(**C**) ADN-HD population coherence remains unchanged. Top: data matched for firing rate (FR). Bottom: baseline-subtracted coherence (Mann-Whitney; U_{Across}=55; p=0.73; U=100; $p < 0.001$ for both conditions compared to baseline).

(**D-F**) Same as (A-C), for bilateral PSB silencing. (Firing rate change: Wilcoxon-signed; W=620; $p < 0.001$; n=114 neurons; ~17% decrease. Coherence: U_{Across}=49; p=0.96; $U_{Chrimson}$=100; $p < 0.001$; $U_{Control}$=100; p<0.001).

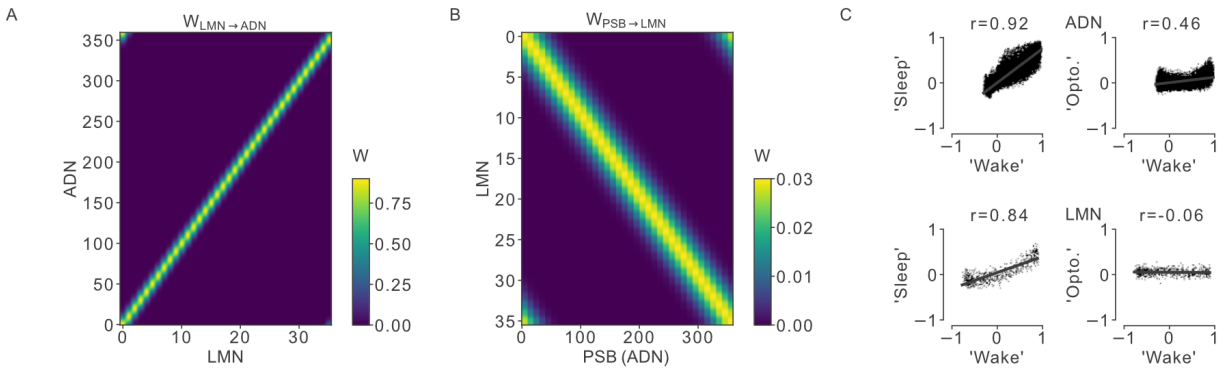

790

791 **Supplementary Figure 8 | Network model details**

792 **(A)** Connectivity matrix for LMN→ADN projections.

793 **(B)** Connectivity matrix for PSB(ADN)→LMN projections.

794 **(C)** Population coherence of LMN and ADN units across conditions: 'wakefulness' vs. 'sleep'

795 and 'wakefulness' vs. 'optogenetic stimulation'.